Midplane measurements of charged fusion product diffusion in the Tokamak Fusion Test Reactor

R. L. Boivin
Plasma Fusion Center, Massachusetts Institute of Technology, 175 Albany St., Cambridge, Massachusetts 02139

S. J. Zweben
Plasma Physics Laboratory, Princeton University, Princeton, New Jersey 08543

(Received 3 September 1992; accepted 11 February 1993)

A radially movable detector located just below the outer midplane of the Tokamak Fusion Test Reactor (TFTR) [in *Plasma Physics and Controlled Nuclear Fusion Research, 1988* (International Atomic Energy Agency, Vienna, 1989), Vol. 1, p. 27] has been used to study the confinement of charged fusion products (CFP's). The scrape-off length of escaping CFP flux was measured using perturbative techniques based on shadowing the detector with different obstacles. Experimental results indicate the presence of a diffusive process for trapped particles. Derived diffusion step sizes were found to be in excellent agreement with those expected from toroidal magnetic field (TF) stochastic ripple diffusion.

I. INTRODUCTION

The transfer of energy from fusion produced alpha particles to the background plasma is essential for sustaining a reaction in an ignited reactor. Any substantial loss or diffusion of particles can jeopardize such self-sustaining reaction. Other potential problems include the possible localization of such losses and thus leading to excessive heat loads on the first wall. This paper describes measurements made near the midplane of TFTR (Tokamak Fusion Test Reactor),[1] on the confinement of charged fusion products (CFP's). In these experiments we studied the cases of the 1 MeV triton and 3 MeV proton, which are normally produced in deuterium only (D–D) plasmas, and which can be used to simulate alpha particle behavior in future reactors with a deuterium and tritium (D–T) mix.

The presence of ripples in the toroidal magnetic field (in this case externally created by the discrete number of toroidal field coils) is theoretically expected to induce diffusion for a significant fraction of trapped charged fusion products.[2,3] Diffusing particles are mainly found near the edge of the plasma (large minor radius) in what is known as the stochastic ripple loss domain (not to be confused with the ripple trapping region).[4] Stochasticity was found to be present when

$$\delta > \delta_s \equiv \left(\frac{\epsilon}{N\pi q}\right)^{3/2} \frac{1}{(2\rho q')}, \tag{1}$$

where δ is the local TF ripple amplitude, N is the number of coils (20 in TFTR), q is the safety factor, ϵ is the local aspect ratio, ρ is the gyroradius, and $q' \equiv dq/dr$. This criterion puts a stringent limit on the maximum ripple strength allowed over the plasma cross section.[4,5]

In that region, trapped CFP's experience, at their bounce point, a random vertical drift (Δr) which scales as

$$\Delta r \propto \left(\frac{N\pi}{|\sin\theta_b|}\right)^{1/2} \left(\frac{q}{\epsilon}\right)^{3/2} \rho\delta \sin(N\phi_b), \tag{2}$$

where all the variables, including the poloidal (θ) and toroidal angles (ϕ), are evaluated at the bounce point.[3,5]

The technique used here for measuring the diffusion rate of CFP's has been previously employed for diffusion studies of runaway electrons.[6] It consists mainly of the insertion of a known obstacle, which creates a shadowed region where perturbed CFP population can be studied using an escaping particle detector. In the absence of diffusion, the shadowed region would be well delimited (e.g., sharp transition boundaries). In the case where diffusion is present, particles gradually fill in the shadowed region. The different techniques of detector shadowing will be described in detail in the following sections.

Experimental results are interpreted using simulation codes based on models which include diffusive mechanisms. Estimates based on the geometry of the experiments will also be used to corroborate the numerical calculations and the applicability of our models. Diffusion step sizes derived from the experimental results and the numerical simulations will then be compared with expectations based on toroidal magnetic field (TF) stochastic ripple diffusion.

II. EXPERIMENTAL TECHNIQUE

The detector is based on a square, thin ZnS scintillator and a system of collimating apertures (slit 1.35 cm×0.7 mm, behind a pinhole 2×0.7 mm), which disperses escaping particles according to their pitch angle (magnetic moment) and gyroradius (from which energy is derived).[7,8] The detector is mounted at the tip of a movable probe located in Bay E, approximately 20° below the outer midplane of TFTR. The present stroke of the probe is 113.7 cm of which 23 cm are within the first wall of the vacuum vessel. Of those 23 cm, the first nine lie in the shadow of the radio-frequency (rf) limiters, which are located in two different bays approximately 117° and 171° away toroidally (in the counter-going direction), and are approximately 50 cm wide toroidally. Precise measurements of the probe position were obtained inside the vacuum vessel during the

 0899-8221/93/051559-08$06.00

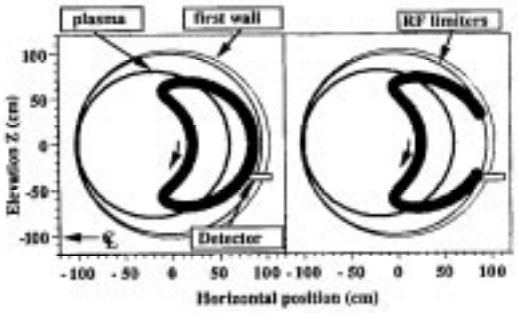

FIG. 1. Typical orbits seen by the detector at two different radial positions, showing the difference between a confined first orbit (left) and an orbit on a direct path to the wall (right).

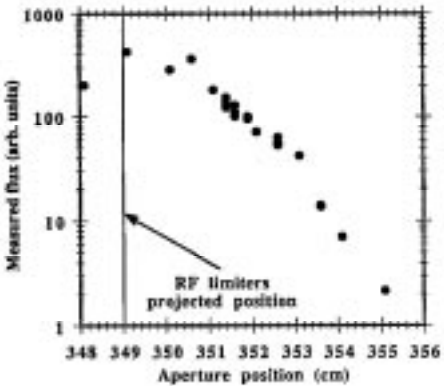

FIG. 2. Aperture radial scan near the outer wall showing the transition from first-orbit confined particles to lost particles. The transition occurs approximately when the aperture passes in front of the rf limiters (at $R_0 \simeq 349$ cm) ($I_p = 1.6$ MA, $B_T = 5$ T, and $R_0 = 2.45$ m).

winter 1991 shutdown with the use of a specially designed articulated measuring arm (with an accuracy of better than 0.3 cm). Additional details of the detector geometry can be found in Refs. 7 and 8.

The probe can be brought very close to the plasma, although it was always kept at a safe distance from the plasma edge ($\gtrsim 5$ cm), since it was not designed to withstand large heat loads. The position of the probe was kept constant during shots, mainly because the driving mechanism is too slow (approximately 0.5 cm/sec), and because the probe position recording was not automated. This ability to move (between shots) enables the detector to look at two different classes of particles, which, on their first orbit (first poloidal transit) are confined or lost, and from now on will be referred as such. In the former case, when the detector is located inside the rf limiters minor radius, there is no other material obstacle between the aperture of the detector and the plasma (except for the detector itself, i.e., self-shadowing). At this location, the detector samples particles on first-orbit confined orbits, or possibly CFP's diffusing out (see Fig. 1). In the latter case, the detector is usually located behind the rf limiters minor radius and detects particle on their direct way to the wall (first-orbit loss, see Fig. 1). Note that since CFP's have large banana widths (30–50 cm, and even more at low current), orbits originating from inside the plasma can bring particles relatively far out from the plasma edge, especially near the outer midplane.

In that region, the CFP escaping flux scrape-off length can be measured independently by using three different obstacles to shadow the aperture (which leads to the scintillator). The first one, seemingly simple, is the detector itself; a cylinder, 6.35 cm in diameter, and approximately 25 cm long and located ~ 35.6 cm below the midplane. The key feature of the probe as an obstacle lies in the position of the aperture (approximately 2 mm^2 in area) which is 3 cm away from the probe tip. This important point will be further discussed below. This is the case of self-shadowing.

The second obstacle is composed of the two rf limiters. They have a relatively flat surface, with a toroidal radius curvature of 155 cm directed outwards, and are 50 cm wide (much larger than the probe), longer than the translation length ($= 2\pi v_\parallel / \Omega \simeq 20$ cm) of a CFP over a gyroperiod. They extend poloidally from the inner bumper limiter, from the top to the bottom along the outer wall ($\theta = \pm 120°$), with a minor radius of 99 cm, almost concentric ($R_{rf} = 260.6$ cm) with the vacuum vessel first wall ($R_{vv} = 265$ cm).

The third obstacle is a Langmuir probe,[9–11] used here as a "dummy" obstacle, and which is similar to the detector in its external dimensions. The Langmuir probe is located above the midplane (36.8 cm above, compared to the detector located at 35.6 cm below) and the head is made of a cylinder 5 cm in diameter and approximately 20 cm long. It is installed at a different toroidal location, in TFTR Bay A, toroidally 72° in the co-going direction. Although the second probe is capable of a fast motion ($\simeq 13$ cm/sec), the results were obtained by changing the obstacle position in between shots only.

III. EXPERIMENTAL RESULTS

In Fig. 2 is shown the measured flux (at a pitch angle of 60°, corresponding to trapped particles) as a function of the aperture radial position in the vicinity of the rf limiters ($I_p = 1.6$ MA, $B_T = 5$ T, and $R_0 = 2.45$ m). Note that, as the aperture is moved further inside the vacuum vessel, the rf limiters block a smaller number of particles and so the detected flux of particles increase substantially. The flux starts to drop at the major radius from which an orbit leads directly to the rf limiters radius at the midplane ($\theta = 0$).

Finally, shown in Fig. 3 are the results of the shadowing experiment done with the second probe in which the aperture of the detector remained at $R_{aperture} = 347$ cm. At this location the effects of the rf limiters are small and the shadowing action is mainly due to the second probe and the detector. In this case, the experimental points correspond to a pitch angle of 55° (also trapped). The conditions chosen for this experiment ($I_p = 1.4$ MA, $B_T = 5$ T, and $R_0 = 2.45$ m) were such that stochastic TF ripple diffusion would be close to its maximum,[8] and that there would be sufficient room between the plasma and the first wall for the probes to maneuver safely.

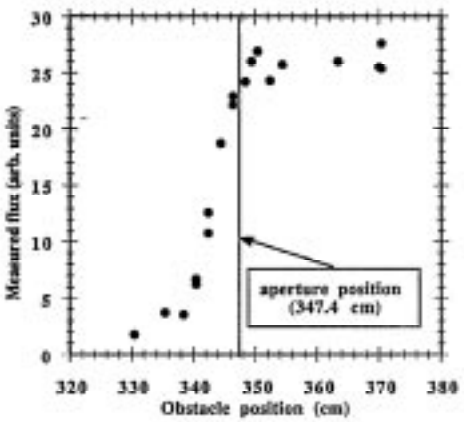

FIG. 3. Experimental results of the shadowing experiment with a second small probe. The second probe (the obstacle) is brought from behind the aperture (aperture located at $R=347.4$ cm), to in front of it.

The obstacle was brought from outside the first wall (approximately 20 cm behind the aperture), to in front of the aperture (approximately 20 cm further in). A very large and relatively sharp decrease of the escaping flux as a function of the obstacle position can be observed. When the obstacle comes close to the aperture radial location, the flux goes down dramatically, and with the full extension of the obstacle, it dropped eventually to only 12% of the original level.

IV. DIFFUSION MODEL

In these experiments, the interaction of obstacles with CFP's is rather complex, mainly because of their large helical orbits (gyroradius of 5–10 cm) and large drifts from their birth flux surfaces (with banana widths of 30–50 cm or more) which are both comparable in dimensions with the obstacles. When the obstacle is sufficiently small (i.e., bay A probe), the orbital effects of the CFP's can be ignored up to a certain degree. In this case, the CFP's do not drift significantly over the diameter of the other probe or the detector. In the case of a larger obstacle (i.e., rf limiters), the CFP's do drift significantly on the scale of the obstacle, both in the toroidal and poloidal directions, and some orbital effects must be included.

Since the measured quantity is the flux of particles at the aperture, the expected flux is computed by following particle orbits backwards in time. An orbit is started at the aperture (with fixed pitch angle and energy, and given gyro and toroidal angles). The particle is stopped when it either hits something (detector, second probe, wall, or rf limiters), or when it goes back deeply in the plasma and reaches the TF ripple stochastic diffusion threshold boundary [see Eq. (1)], for example. For each poloidal transit before the final impact (or before the particle returns deeply into the plasma), a counter is incremented by the magnitude of the CFP source profile for particles born on that orbit.

In the case where an obstacle is gradually brought in (i.e., second movable probe) the fluxes are compared using a scheme shown in Fig. 4. In the presence of an obstacle,

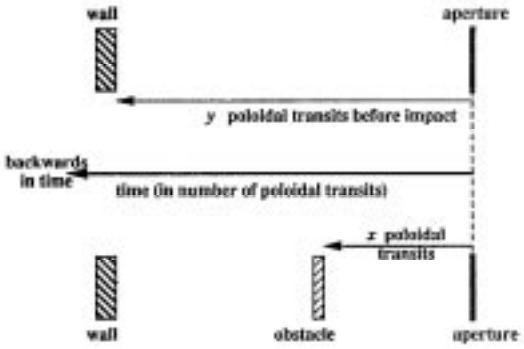

FIG. 4. Comparison between cases with an obstacle (bottom) and without (top), showing the difference in flux to the aperture. In the example without the obstacle, the particle would impact on the wall. In the bottom case the flux would be reduced by a factor of x/y from the top case.

the flux to the aperture will be reduced since the orbital line of sight is now blocked somewhere along the original orbit. A schematic rendition of an original orbit is shown at the top of Fig. 4, where a particle eventually hits the obstacle (e.g., a wall). In the case illustrated at the bottom, the presence of an obstacle was added, and the particle is consequently stopped before hitting the wall. In this scheme the particle makes x poloidal transits instead of y, before being stopped. The flux of particles to the detector is the integral (from the source profile) of CFP's born on that orbit (with a given energy and magnetic moment), which can be composed of many poloidal transits. Each poloidal transit corresponds to a given integrated number of particles. The flux would be then proportional to the number of poloidal transits. Consequently, the flux to the aperture, in presence of an obstacle, would be approximately x/y times the flux detected without the presence of an obstacle. It is important to note that the transit time is much faster ($-\mu$sec) than any collisional time ($\sim$sec) and thus collisions can be neglected.

The error bars of the numerical simulation also include uncertainties arising from our specification of the boundary conditions. Outlined in Table I are the principal characteristics of the three models discussed above, and will be described in more details in the next three sections.

TABLE I. Relative characteristics for the different shadowing experiment models.

Model	Self	Large obstacle	Small obstacle
Obstacle	detector only	rf limiters	Probe A
Obstacle size	small $\simeq$gyroradius	large (toroidally and poloidally) many gyroradius	small (similar poloidal location) $\simeq$detector
Probability of impact	small	large	small
Gyroradius (FLR) effects	yes	no	yes
Orbit details	negligible	important	negligible
Toroidal location	random	following orbit	random
Self shadowing	included	included	included

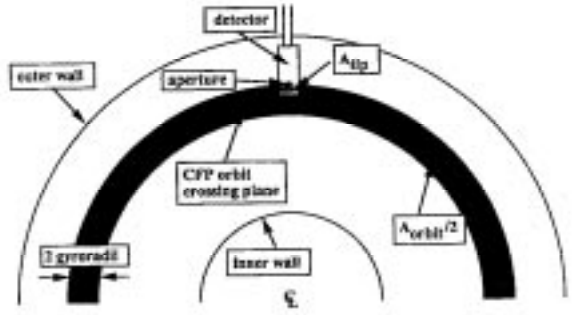

FIG. 5. Toroidal cross section of the tokamak showing the detector and the region where the orbit intersects the toroidal plane at the elevation ($Z=-35.6$ cm) of the aperture. The probability of impact per poloidal transit would be approximately the ratio of the projected areas A_{tip}/A_{orbit}.

A. Detector self-shadowing

First of all, it is important to quantify theoretically the effects of the presence of the detector. In the region where the detector samples confined ions, the finite dimension of the detector can affect its own detection efficiency. Particles, which are orbiting for many toroidal transits, can be blocked by the detector structure before penetrating the aperture. Thus, the aperture cannot see particle orbits going backwards in time further than the time between two impacts. Estimates of the time of impact can be obtained using considerations based on the detector dimensions. These estimates will be corroborated in the next sections with the use of numerical calculations.

Shown in Fig. 5 is the toroidal cross section of the tokamak (top view) taken at the elevation ($Z=-35.6$ cm) of the aperture. In this case, only the detector is present, and the particles are not diffusing ($D=0$). Consequently, for each poloidal transit, when the particle is at the same elevation (or Z position) than the aperture/detector, the particle will be somewhere in the shaded toroidal band of two gyroradii (ρ) in width. Assuming that the toroidal angle is random (no resonance), the probability of self-shadowing would be simply the ratio of the toroidally projected area of the detector over the total surface of the orbit band. In other words, for each poloidal transit the detector will catch a fraction of particles equivalent to A_{tip}/A_{orbit}. On the average, between 500 and 1000 poloidal transits (or simply, twice as many bounce times) are necessary before a particle started at the aperture of the detector (backwards in time) impacts on the probe head. This would mean that in the absence of diffusion, the aperture can only look back in time approximately 1000 to 2000 bounce times, about 10 to 20 msec ($\tau_b \simeq 10$ μsec for the 1 MeV triton), before it hits the detector. Note that this time scale is still very fast compared to the slowing down time ($\simeq 1$ sec) and so collisional effects between particles can be safely neglected.

In order to measure diffusion rates using this technique, particles must diffuse at least 3 cm (distance between the tip and the aperture) in less than the calculated 1000 to 2000 bounce times between successive impacts. Particles are detected only at the aperture, and if particles are diffusing too slowly, they would be scraped-off by the probe head tip before reaching the aperture. For a 1 MeV triton, this means that the diffusion rate must be larger than $(3\text{ cm})^2/10\text{ msec} \sim 0.1\text{ m}^2/\text{sec}$, which is low enough for the study of TF ripple diffusion (by at least an order of magnitude).

B. Diffusion in the presence of a large obstacle

When in the presence of the two rf limiters, one must take in account some details of the actual particle trajectory near the outer wall. Since limiters have broad poloidal and toroidal extensions, particles can impact the limiters at many locations. When the aperture is positioned well inside the radius of the rf limiters (in the confined particle region), the CFP flux would be limited by the detector self-shadowing. On the other hand, when the aperture is outside the radius of the rf limiters, the flux would be largely reduced by the limiters due to their relatively large size.

In the numerical simulation used to interpret the results of Fig. 2, particles were started at the aperture. From there, the bounce point is found using a modeled banana orbit derived from time-reversed calculations made by ORBIT.[12] Diffusion is then applied to the radial position of the particle bounce point using Eq. (2) as the step size. The banana orbit is then followed (using the modeled orbit) until the particle either hits an obstacle (rf limiters or the detector) or reaches the upper bounce point. Diffusion of the bounce point continues until an impact occurs. There is also a small probability for the particle to return to the center of the plasma; those particles are simply stopped when they are found to be near the TF ripple stochastic threshold boundary [Eq. (1)]. As in the previous case, the flux to the aperture is consequently proportional to the number of poloidal transits before a particle impacts on an object (detector or limiters) or before it reaches the TF ripple stochastic threshold boundary. The numerical results were found to be relatively insensitive to changes in boundary conditions (i.e., with possible variations in the threshold boundary location) as indicated by the error bars of the numerical curves in Fig. 6.

One immediate result of these calculations is related to the question of detector self-shadowing discussed in Sec. IV A. In the absence of diffusion, when the aperture is much further inside than the radius of the rf limiters, it was found numerically that the particle takes between 800 and 1000 bounce times (or 1600 to 2000 poloidal transits) before impacting the detector. This is in good agreement with the estimates derived in the previous section.

Comparison of the numerical calculations with the experimental results are shown in Fig. 6. All curves are normalized to the $R_{aperture}=349$ cm point, where the limiters play a minimal role. The difference between the experimental curve and the no-diffusion case is especially important. In the absence of diffusion, particles are either blocked or not by the limiters. The reasons for the calculated sharp fall-off (with $D=0$) are twofold. First, the particles travel on a long distance toroidally near the outer wall ($\Delta\phi$

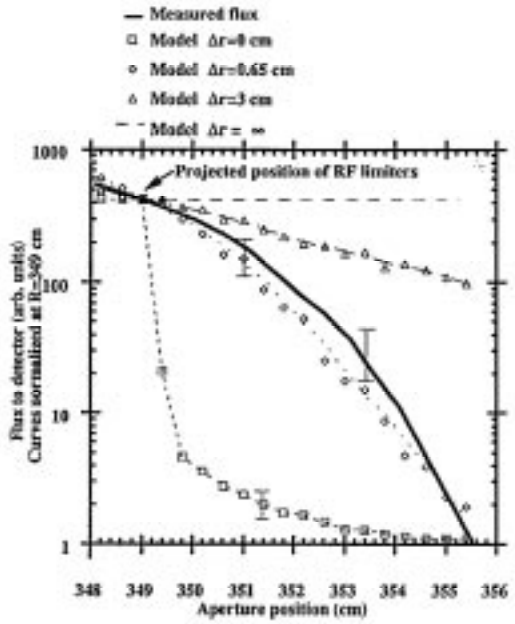

FIG. 6. Comparison of the experimental results (at $\chi \simeq 60°$) of the aperture radial scan with the theoretical model including TF ripple diffusion. Also shown is the no-diffusion case with the expected sharp transition at the rf limiters radius.

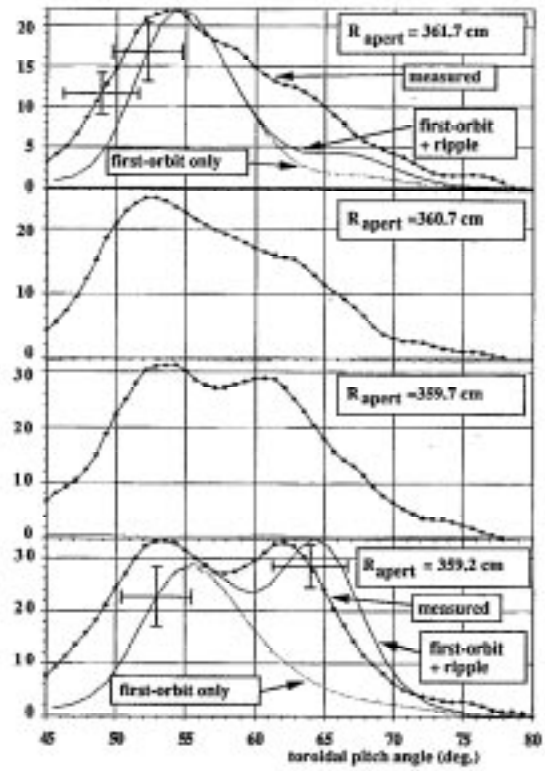

FIG. 7. Measured pitch angle distributions during partial aperture radial scan behind the rf limiters. Experimental curves have been normalized by the neutron production, and the camera gain remained the same. The ripple peak (right) doubles in amplitude whereas the first-orbit peak (left) increases only slightly. Also shown are the numerical calculations (top and bottom), which include both loss mechanisms.

$=q\Delta\theta$), and are likely to hit the limiters when their radial excursion brings them behind the rf limiter radius. Second, the rf limiters are wider than the translation length of a CFP (distance along a field line over a gyroperiod) eliminating any gyroradius effect.

For the different diffusion cases shown, the parametric dependence of Eq. (2) was used, and the step size amplitude was varied using a global factor. With increased diffusion step size, proportionally more particles are slipping behind the limiters. The best fit was found with $\Delta r = 0.65 \pm 0.2$ cm ($\Diamond$) (at $R_{\text{aperture}} = 349$ cm). On the other hand, if the step size is increased further (to $\Delta r \simeq 3$ cm, Δ), the large drop in flux cannot be replicated. And in the extreme limit ($\Delta r \to \infty$, dashed line), the limiters would simply have no effect on the measured flux.

Using orbit retracing (i.e., code ORBIT[12]), the expected TF ripple diffusion step size was calculated using Eq. (2). For particles at this pitch angle, energy, and minor radius, Δr was found to be 0.75 ± 0.2 cm, in very good agreement with the experimental results shown above.

The effects of the rf limiters were also investigated by looking at the escaping particle pitch angle distribution as a function of the detector's position. Conditions were chosen such that first-orbit and ripple features were visible during the same discharge ($R_0 = 2.60$ m, $I_p = 1.4$ MA, 3.5 T). Shown in Fig. 7 are the measured pitch angle distributions for the radial scan, in which the aperture was moved radially inwards, away from the wall (over 3.5 cm). The same normalization was kept for the measured distributions (normalized by the source strength and for the same camera gain). Superimposed are the expected distributions at the wall for first-orbit and ripple losses, calculated for the first and last cases, in which the wall was positioned at the aperture position. In this scan the first-orbit peak increases only slightly, whereas the ripple peak doubles in amplitude. This difference in behavior for the two peaks is easily understood when we compare it to the numerical simulations of Fig. 6. The flux in first-orbit losses (e.g., no diffusion curve) changes very slowly with position, whereas the ripple (e.g., with diffusion curve) losses increase more rapidly.

C. Diffusion in the presence of a small obstacle

When using the Bay A probe as an obstacle, the reduction in flux was found to be important but not as drastic as in the case of the rf limiters (see Fig. 3), and this, mainly because of the much smaller size of the other probe.

The aperture of the detector was positioned inside the rf limiters radius, so as to reduce problems associated with the boundary conditions (walls, limiters). Since both probes are in a similar poloidal location and are of similar dimensions which are small compared to the CFP orbit (i.e., banana width), most details of the orbits can be neglected.

As a first approximation, the detector can be seen as a two-dimensional object with radial and toroidal extensions,

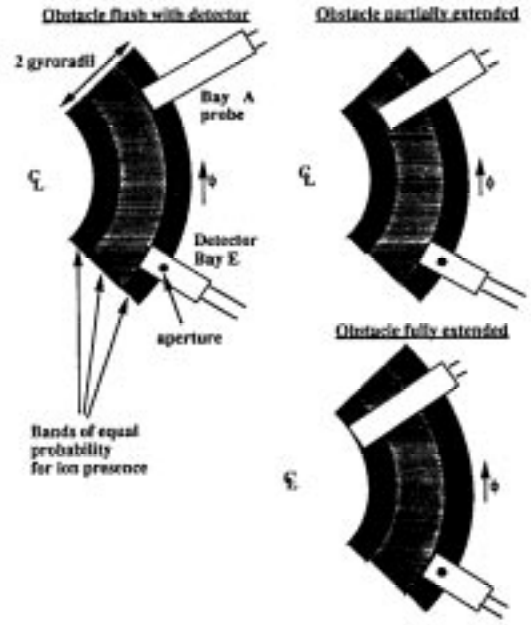

FIG. 8. Toroidal projection of the shadowing experiment with the Bay A probe (a Langmuir probe, located above the midplane) used as an obstacle. The obstacle is shown here at three different locations cutting progressively flux to the detector's aperture. The three different zones in the orbit band represent regions of equally probable presence of a CFP.

eliminating the poloidal dimension. The obstacle and the detector are simply projected onto a toroidal plane, as in Fig. 5.

Before comparing the numerical calculations and the experimental results, basic estimates can be made based on sustained area, as in the previous section. Again, let us start the case with no diffusion. Since the aperture is inside the radius of the rf limiters, the detector lies in the confined CFP region. In Fig. 8, a portion of the particle orbit is projected onto a toroidal cross section showing the detector and the obstacle (same basic approach than in the self-shadowing case). As in Fig. 5, the orbit is represented by a band with a width of 2 gyroradii (ρ), divided in three sections of equal particle location probability. The band is conveniently divided in three, since the detector tip protrudes 3 cm into that band (the distance between the aperture and the tip of the detector) and covers the first zone. This distance is also, coincidentally, approximately half the particle gyroradius. The band stops at the aperture and represents the range of orbits that can be detected. The relative probability for the particle to hit either the detector or the obstacle is thus proportional to their respective area present in the orbits band.

Shown in Fig. 5 are the cases in which the obstacle is covering the three different zones. In the first case, the detector and the obstacle are equally distant and cover the first zone of the orbit band. Consequently, the flux to the detector should be roughly $A_{\text{detector}}/(A_{\text{obstacle}}+A_{\text{detector}}) \simeq 0.54$ times the flux without the obstacle. (Here, A_i is the projected area of the detector or the obstacle and $A_{\text{obstacle}}/A_{\text{detector}}=5/6$.) At that point, the obstacle tip has moved 3 cm past the detector aperture. In the second case, the obstacle moved over the second zone. The flux to the aperture is then proportional to $A_{\text{detector}}/(2A_{\text{obstacle}}+A_{\text{detector}}) \simeq 0.37$ times the flux without the obstacle. In the final case, the flux to the aperture is further reduced, this time it would be $A_{\text{detector}}/(3A_{\text{obstacle}}+A_{\text{detector}}) \simeq 0.28$ times the flux without the obstacle. In the absence of diffusion, this flux level would be the lowest possible. If one moves the obstacle further in, the obstacle does not block more particles present in the band. It would simply block particles that cannot reach the aperture. However, the situation would be different with the presence of diffusion, as the obstacle could block particles long before they can be detected. In order to quantify the effects of diffusion though, numerical calculations are necessary.

As in the other numerical model, the particles are started at the aperture and followed backwards in time using their guiding-center location near the detector or the obstacle. For each poloidal transit ($=2\tau_b$), the particle would return at the detector poloidal location (which is not spelled out explicitly). The toroidal location ϕ_i is determined randomly, and the radial position $r_{\text{particle},i+1}$ is determined through the position of the guiding center $r_{\text{gc},i}$ and a random gyroangle α_{i+1}. The basic iteration scheme can be summarized as follows:

$$\begin{aligned} r_{\text{gc},i+1} &= r_{\text{gc},i} + \Delta r(r_{\text{gc},i},\phi_i), \\ r_{\text{particle},i+1} &= r_{\text{gc},i+1} + \rho\cos(\alpha_{i+1}). \end{aligned} \tag{3}$$

The diffusion process is applied to the guiding center position, but the true random variable is the gyroangle, not the radial position itself. This effect is crucial, because, when the orbit is projected on the toroidal plane of the aperture, the particle has a larger probability to be at the extremes in r. In other words, the radial distribution of the particle's location probability is not uniform but scales as $\sin^{-1}(r/\rho)$. Finally, $\Delta r(r_{\text{gc},i},\phi_i)$ is the step size corresponding to Eq. (2) and is the only free parameter of the fit with the experimental results. Corrections for the orbiting particle pitch angle and the poloidal extension of the obstacle were introduced to increase the accuracy of the numerical model. However, these corrections were found to change the results by only 15% above the previous estimates.

Using the scheme shown in Fig. 4, the comparison shown in Fig. 9 is between the numerical calculations and the experimental results. All curves are normalized at $R_{\text{obstacle}}=370$ cm, corresponding to the obstacle being completely retracted. The experimental vertical error bars are indicative of the shot-to-shot variations, whereas the horizontal ones correspond to the uncertainty in the detector/obstacle position.

Discussed first is the case with no diffusion, as shown in Fig. 9 (□). Here, particles are confined and stay fixed to the same flux surface. In this case the estimated flux levels based on area considerations alone are recovered. With slightly increased diffusion rate (i.e., for $\Delta r \lesssim 0.05$ cm), the

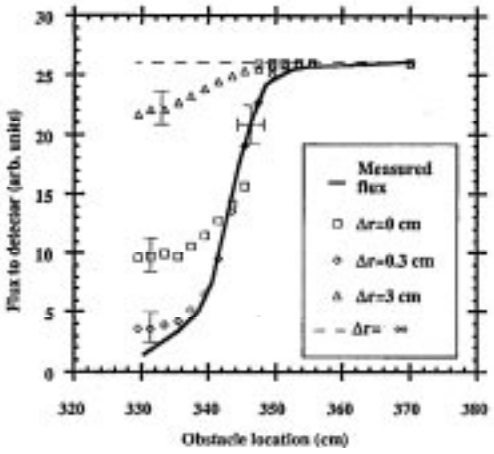

FIG. 9. Measurements and calculations of the radial fall-off the escaping flux as a function of the obstacle position. The experimental results, shown by a continuous line are compared to numerical calculations involving different diffusive step sizes. All the calculated curves are normalized at the $R_{obstacle}=370$ cm point.

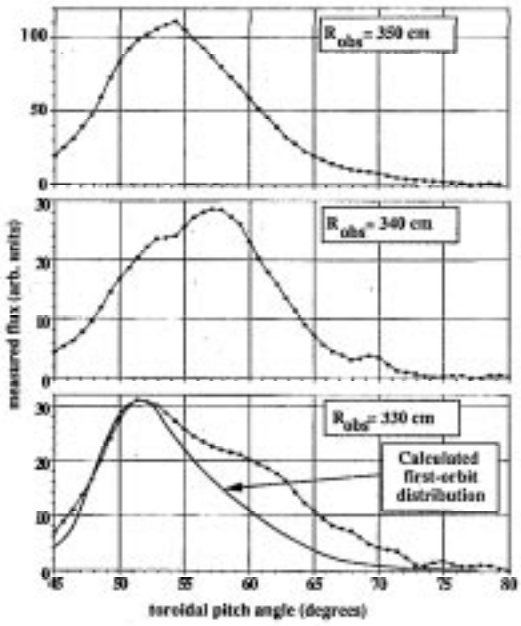

FIG. 10. Measured pitch angle distributions obtained with the probe A (small obstacle) located at different radial positions (top: $R_{obstacle}=350$ cm, middle: $R_{obstacle}=340$ cm), bottom: $R_{obstacle}=330$ cm. First-orbit losses become predominant (lower pitch angles) as diffusing particles were progressively blocked by the obstacle. Also in the bottom case are calculations from ORBIT with the expected first-orbit loss distribution. The camera gain has been increased by a factor of 3 in the bottom case (all with same neutron production).

obstacle still does not block more particles than in the no diffusion case. The reason is that in this case, particles would not diffuse fast enough to reach the aperture before being scraped off by the tip of the detector. In other words, at low diffusion rate, self-shadowing is dominant (see Sec. IV A for the self-shadowing case).

With further increased diffusion rate, here for $\Delta r=0.3$ cm ($\Diamond$), the particles have a much larger probability to hit the obstacle before they can reach the aperture. In other words, they diffuse fast enough to avoid hitting the tip of the detector, but in the meantime, not enough to avoid being blocked by the obstacle, especially when the obstacle is located very far inside the aperture (e.g., by ~ 15 cm). This step size corresponds to the best numerical fit with the experimental results. By considering the uncertainty in the measurements and in the model, the experimentally obtained step size is restrained to be between 0.2 and 0.4 cm.

Finally, with a large rate, here $\Delta r=3$ cm (Δ), the particles are diffusing too fast, the obstacle does not have the opportunity to efficiently block particles before reaching the aperture. The position of the obstacle becomes less and less important, as the particles are moving out more and more rapidly. In the limiting case of $\Delta r\rightarrow\infty$, the curve would simply become a simple horizontal straight line (shown in the figure with a dashed line); the obstacle would not block any particle. That case would be similar to the detection of first-orbit losses, the obstacle would not be able to block any particle since they would be lost in a very fast time scale. The pitch angle distribution would follow a first-orbit loss distribution, an unobserved characteristic (see, for example Fig. 10).

The experimentally obtained step size can be compared with the one expected theoretically by using Eq. (2) and the orbit code ORBIT.[12] By retracing the orbit from the aperture to the bounce point (which gives us r_b and θ_b for evaluating Δr) it was found that Δr should be 0.3 ± 0.1 cm, in very good agreement with the obtained result. The uncertainty in the theoretical value of the step size being mainly due to the uncertainty in $q(r)$.

The effects of a progressive shadowing are also visible in the pitch angle distribution. In the absence of diffusion, the maximum flux comes at the fattest banana pitch angle, which corresponds to the orbit which comes the closest to the plasma center. When a diffusing process is present, the distribution will exhibit the presence of an additional peak at higher pitch angle. In this case the detected flux is dominated by diffusing particles. However, the obstacle is more efficient in blocking diffusing particles than confined particles ($D=0$), if it is placed sufficiently ahead of the aperture. That difference in "blocking efficiency" is visible in the numerical simulations of Fig. 9, where $\sim 63\%$ of the flux is blocked if the particles are not diffusing, and more than 80% if they are. Consequently, when the obstacle is positioned well in front of the aperture, the pitch angle distribution should change. In Fig. 10 the pitch angle distribution is shown for three different obstacle positions. At the maximum obstacle extension, the distribution is largely shifted towards the pitch angle of the fattest banana, in this case located at $\chi\simeq 49°$. In the case shown (bottom graph), the first-orbit loss distribution has been calculated using ORBIT.[12]

However, the pitch angle distribution does not change monotonically with the obstacle position. When the obstacle is inserted further in, the peak of the distribution briefly moves to higher pitch angles (middle curve, in Fig. 10)

and then moves down to lower pitch angles (i.e., the bottom case in Fig. 10). This behavior is believed to be a manifestation of different diffusion rates for different pitch angles. Recall that the step size is a strong function of the ripple amplitude (which depends on the minor radius and the poloidal angle) so diffusion rates will change with the bounce point location. For example, from the location the bounce point of different pitch angle particles (using the orbit code), theoretically, at $\chi \simeq 50°$ the particle is out of the stochastic area ($\Delta r = 0$). For particles detected at $R_{\text{aperture}} = 353$ cm, we have that with $\chi = 55°$, $\Delta r = 0.3$ cm, and with $\chi \simeq 60°$, $\Delta r = 0.7$ cm. Particles with a small diffusion rate ($\chi \sim 55°$) would be cut first (as in the middle curve of Fig. 10) then the ones with a larger diffusion rate ($\chi \sim 60°$) leaving the first-orbit losses only (as in the bottom curve). Unfortunately, the detector resolution in pitch angle is not sufficiently good for a complete deconvolution of the different diffusion rates.

V. CONCLUSION

Different experiments based on detector shadowing techniques have been used to measure the diffusion rate of charged fusion products near the outer midplane of TFTR. These measurements, made on trapped particle populations, showed the presence of a relatively large diffusion mechanism $(\Delta r)^2/\tau_b \sim (1\text{ cm})^2/10\ \mu\text{sec} \approx 10\ \text{m}^2/\text{sec}$. Numerical simulations based on orbital and geometrical considerations were used to infer the diffusion step sizes and the results obtained were successfully compared with simple estimates made by using area and geometrical arguments. The amplitude of the diffusion step sizes were also compared with theoretically expected TF stochastic ripple diffusion rates. The agreement was found to be very good, well within the experimental uncertainties. Although the diffusion rate is found to be high, the number of TF stochastic ripple diffusing particles is believed to be small[8,13,14] and should not affect ignition. However, even a small number of lost particles could create heat load problems, if they are sufficiently localized on the first wall. These results complement other measurements made in TFTR, using the same probe for the study of CFP diffusion but which were mainly based on the pitch angle resolution capabilities of the detector. They focused directly on the study of the stochastic threshold and on the lost particles distribution at the first wall. They were also found to be consistent with the presence of TF stochastic ripple diffusion mechanism especially with respect to the presence of a stochastic domain.[8,13,15]

ACKNOWLEDGMENTS

We thank the TFTR group for their support, especially of S. Cohen, R. Hawryluk, S. Kilpatrick, D. Manos, K. McGuire, D. Meade, and K. Young. We would like to acknowledge the valuable contributions of M. Diesso, R. Goldston, G. Hammett, H. Mynick, S. Scott, and J. Strachan in the interpretation of the results.

One of us (R.B.) wishes to thank the Natural Sciences and Engineering Research Council of Canada (NSERC) for its financial support during this research. This work was supported by U.S. Department of Energy Contract No. DE-AC02-76-CHO-3073.

[1] M. Bell, V. Arunasalam, C. Barnes, M. Bitter, H.-S. Bosch, N. Bretz, R. Budny, C. Bush, A. Cavallo, T. Chu, S. Cohen, P. Colestock, S. Davis, D. Dimock, H. Dylla, P. Efthimion, A. Erhrardt, R. Fonck, E. Fredrickson, H. Furth, G. Gammel, R. Goldston, G. Greene, B. Grek, L. Grisham, G. Hammett, R. Hawryluk, H. Hendel, K. Hill, E. Hinnov, J. Hosea, R. B. Howell, H. Hsuan, R. A. Hulse, K. Jaehnig, A. Janos, D. Jassby, F. Jobes, D. Johnson, L. Johnson, R. Kaita, C. Kieras-Phillips, S. Kilpatrick, V. Krupin, P. LaMarche, W. Langer, B. LeBlanc, R. Little, A. Lysoyvan, D. Manos, D. Mansfield, E. Mazzucato, R. McCann, M. McCarthy, M. McCune, K. McGuire, D. McNeill, D. Meade, S. Medley, D. Mikkelsen, R. Motley, D. Mueller, J. A. Murphy, Y. Murakami, E. B. Neischmidt, D. K. Owens, H. Park, A. T. Ramsey, M. H. Redi, A. L. Roquemore, P. H. Rutherford, T. Saito, N. R. Sauthoff, G. Schilling, J. Schivell, G. L. Schmidt, S. D. Scott, J. C. Sinnis, J. Stevens, J. D. Strachan, B. C. Stratton, W. Stodiek, G. D. Tait, G. Taylor, J. R. Timberlake, H. H. Towner, M. Ulrickson, S. von Goeler, R. Wieland, M. Williams, J. R. Wilson, K.-L. Wong, S. Yoshikawa, K. M. Young, M. C. Zarnstorff, and S. J. Zweben, in *Plasma Physics and Controlled Nuclear Fusion Research 1988*, Proceedings of the 12th International Conference, Nice (International Atomic Energy Agency, Vienna, 1989), Vol. 1, p. 27.

[2] R. J. Goldston and H. H. Towner, J. Plasma Phys. **26**, 283 (1981).

[3] R. J. Goldston, R. B. White, and A. H. Boozer, Phys. Rev. Lett. **47**, 647 (1981).

[4] R. B. White and H. E. Mynick, Phys. Fluids B **1**, 980 (1989).

[5] R. B. White, *Theory of Tokamak Plasmas* (North-Holland, Amsterdam, 1989).

[6] J. D. Strachan, Nucl. Fusion **16**, 743 (1976).

[7] R. L. Boivin, S. Kilpatrick, D. Manos, and S. J. Zweben, Rev. Sci. Instrum. **61**, 3208 (1990).

[8] R. L. Boivin, PhD thesis, Princeton University, Princeton, New Jersey, 1991.

[9] D. Manos, R. V. Budny, S. Kilpatrick, P. Strangeby, and S. Zweben, Rev. Sci. Instrum. **57**, 2107 (1986).

[10] D. M. Manos and S. J. Kilpatrick, *Proceedings of the Material Research Society Symposium, Reno, 1988*, edited by A. K. Hays (Materials Research Society, Pittsburgh, 1988), Vol. 117, p. 263.

[11] S. J. Kilpatrick, D. M. Manos, R. V. Budny, P. C. Strangeby, R. S. Ritter, and K. M. Young, J. Vac. Sci. Technol. A **4**, 1817 (1986).

[12] J. Felt, C. W. Barnes, R. E. Chrien, S. A. Cohen, W. W. Heidbrink, D. Manos, and S. Zweben, Rev. Sci. Instrum. **61**, 3262 (1990).

[13] R. L. Boivin, S. J. Zweben, and R. B. White, "Study of stochastic toroidal field ripple losses of charged fusion products at the midplane of TFTR," Nucl. Fusion **33** (1993) (to be published).

[14] D. E. Post, K. Borrass, J. D. Callen, S. A. Cohen, J. G. Cordey, F. Engelmann, N. Fujisawa, M. F. A. Harrison, J. T. Hogan, H. J. Hopman, Y. Igitkhanov, O. Kardaun, S. M. Kaye, S. Krasheninnikov, A. Kukushkin, V. Mukhovatov, W. M. Nevins, A. Nonentini, G. W. Pacher, H. D. Pacher, V. V. Parail, L. D. Pearlstein, L. J. Perkins, S. Putvinskij, K. R. D. J. Sigmar, M. Sugihara, D. Swain, T. Takizuka, K. Tani, T. Tsunematsu, N. A. Uckan, J. G. Wegrowe, J. Wesley, S. Yamamato, R. Yoshino, K. Young, P. N. Yushmanov, and International Contributors, *ITER Physics*, ITER Documentation Series No. 21 (International Atomic Energy Agency, Vienna, in press).

[15] R. L. Boivin, S. J. Zweben, C. S. Chang, G. Hammett, H. E. Mynick, and R. B. White, *Proceedings of the 18th European Conference*, Berlin, 1991 (European Physical Society, Geneva, 1991), Vol. 1, p. 49.